

Modeling and Simulation of Fuzzy Logic Controlled Pulse Density Modulation for Bidirectional Inductive Power Transfer

Pentapalli s sampath vinayak¹, Balabomma bhaskara rao²

 $^{\rm 1}$ PG Student , EEE & Sankethika Vidya parishad College of Engineering, Visakhapatnam

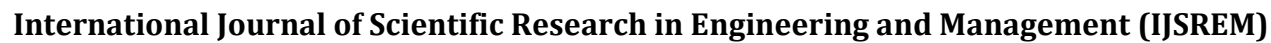
² Assistant professor OF EEE Department, EEE & Sankethika Vidya parishad College of Engineering, Visakhapatnam

ABSTRACT

By enabling seamless Grid to Vehicle (G2V) and Vehicle to Grid (V2G) operations, the new bidirectional wireless power transfer (BWPT) technology offers greater flexibility without the need for human involvement. However, power factor management, efficiency, and power transfer rate are problems with BWPT systems. Advanced control systems are necessary to solve these problems. Bidirectional systems need dual-side management of power converters to effectively handle G2V and V2G activities, although unidirectional Wireless Power Transfer (WPT) can be effectively managed by traditional control techniques and power factor corrector (PFC) procedures. Additionally, the body of current literature primarily concentrates on increasing power factor for unidirectional WPT systems. In order to improve PFC control for BWPT, this research proposes a dual-phase shift Pulse Width Modulation (PWM) approach. The proposed method is thoroughly examined, with particular attention paid to power factor, bifurcation, total harmonic distortion (THD), and power losses. The effectiveness demonstrated system's is simulation studies. experimentation, and verification conducted at an operating frequency of 85 kHz and a power rating of 3.7 kW. In both power directions. dual-phase transfer shift control produces simulated results with 94.4% power transfer efficiency and experimental findings with 90.1%.

I. OVERVIEW

The emergence of new energy issues driven by environmental concerns and the depletion of fossil fuels has a substantial impact on the automotive industry. This result has spurred additional research and development in the EV sector [1]. EV recharge is one of the most crucial problems that must be fixed to promote industry growth. Recharge time, safety, and human interaction are the three biggest challenges with EV charging. To get around these problems, the recently created Because WPT technology delivers electricity from a source to a load without making physical touch, it is crucial [2]. WPT provides the user with significantly more comfort and security than traditional wire charging. Since charging cords are no longer necessary thanks to this technology, charging is now safer and more convenient. Because human intervention-free charging capabilities reduce battery size and weight and charging intervals, users can charge smart devices anywhere there is a charging outlet [3]. Additionally, WPT technology finds utility in highpower applications including as railroad traction, underwater vehicles, and wirelessly energizing medical implants [4], [5]. It's not restricted to charging EVs. WPT is important because it may overcome the drawbacks of battery-powered gadgets, namely as limited battery life and high initial costs. WPT's features, such as dependability, convenience, safety, and weather resistance, have made it more appealing [6]. In particular, it is anticipated that the application of BWPT will hasten the development of V2H, V2V, and V2G technologies, enabling bidirectional





SJIF Rating: 8.586

electrical flow. The design of the WPT/BWPT systems incorporates completely regulated switching components, such as SIC MOSFETs and IGBTs, allowing high frequency operation for both the primary as well as secondary bridges. Figure 1 displays the standard block diagram that illustrates the interactions between photovoltaic (PV) systems, wirelessly connected EVs, a DC bus, and the power grid in V2G and G2V operations. By improving power quality and grid stability through active or reactive power correction, EVs support the electrical grid [7].

EVs, the power grid, and Renewable Energy Systems (RES) can all be integrated to efficiently boost RES adoption [8]. However, during charging and discharging conditions, this integration necessitates continuous bidirectional communication.

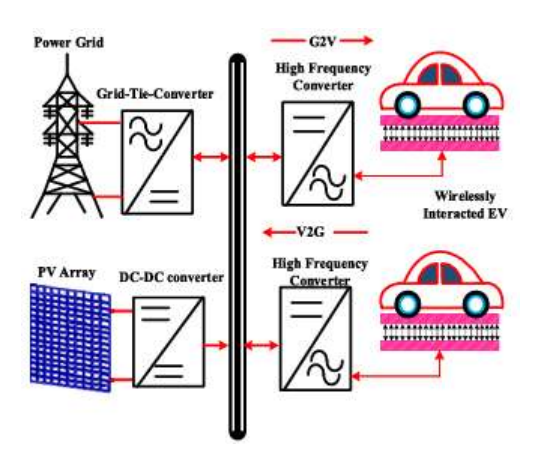


FIGURE 1. Illustration of wirelessly interconnected EVs in the V2G and G2V service.

The grid-connected system must keep the power factor and THD within the permitted range. Additionally, the wireless charging system's power electronic converters are essential to preserving power quality. Misalignment, parameter detuning, coil distance fluctuation, and load variation are some of the uncertain scenarios that cause the WPT system to deviate from its typical behaviour [9]. Additionally, it reduces component stress, power factor, soft switching loss, and power transfer efficiency. However, in order for the BWPT system to preserve grid integration, the power factor is more crucial. Therefore, it is crucial for the wireless charger design to maintain a greater power factor. On the other side, employing appropriate resonance compensation can increase the power transfer efficiency. networks at the primary as well as secondary [10]. To maintain the voltage and current

variation, a variety of compensation topologies are suggested for the unidirectional Compensating tanks are typically added to the AC links of the two bridges to boost system transmission efficiency and capacity. symmetrical construction and reduced sensitivity to load variation and coupling coefficient of the LCC-BWPT system have attracted attention [11]. On the primary side, issues brought on by S compensation are mitigated by the LCC compensation architecture [12]. The LCC resonance compensation circuit on the primary side prevents overcurrent issues related to S compensation by using an inverter to convert a voltage source into a current source. This maintains a steady current in the primary coil. Furthermore, even under The LCC resonance correction circuits help to raise the output voltage under light loads. In conventional BWPT, the direction and amount of actual and reactive power flows are controlled by the relative phase angle and amplitude of the voltages generated by full-bridge inverters on the main and secondary sides [13]. These inverters' switching signals can be synchronized via wireless communication interfaces, however doing so reduces system robustness and increases system costs. By utilizing the active and reactive power of the secondary side's full-bridge inverter for synchronization, an alternative control method eliminates the need for wireless communication [14], [15]. The properties of the passive components and the relative phase angle continue to dictate the real and reactive power flows. as well as the voltage magnitude from the two sides' full-bridge inverters. In wireless circuit designs, recent developments have moved from single-sided to double-sided compensation, offering more flexibility satisfying WPT system design requirements. [15]

ISSN: 2582-3930

Power regulation from unregulated AC output to regulated DC output is essential for WPT systems running at higher frequencies, particularly when charging EV batteries. To improve system power density in this regard, integrated power factor correction (PFC) circuits have been suggested as an alternative to conventional front-end PFC circuits, which frequently call for large passive components [16]. Although the potential impact on battery life, it is projected that integrating EVs with other resources will benefit grid operators and EV owners monetarily. Power Factor Correction (PFC) has



International Journal of Scientific Research in Engineering and Management (IJSREM)

Volume: 09 Issue: 10 | Oct - 2025

SJIF Rating: 8.586

been used to the secondary side of a WPT system in order to increase overall system cost-effectiveness [17]. It's important to recognize, nevertheless, that this method adds more circuit complexity [2]. The importance of the LCCL compensation topology in preserving a steady output voltage on the secondary side is highlighted by the control strategy implemented for the secondary side of a WPT system using an LCCL network. In a similar vein, stability is essential for effectively controlling the linked DC-DC converter that charges batteries [3]. To control A hybrid Inductor Capacitor-Capacitor-Series (LCC-S) compensated technique is used to adjust the output voltage in a WPT system [18]. Phase shift modulation combined with This method, called the LCC-S compensated WPT, enables widerange output voltage regulation throughout the whole voltage range using a switch-controlled capacitor [4], [18], and [19]. A 500-W prototype with an input voltage of 400 V and an output voltage of 100-250 V was put together for validation. According to experimental data, the converter achieves a maximum efficiency of 94.1% and maintains Zero Voltage Switching (ZVS) over the voltage range [19]. To generate load-independent Constant Voltage (CV) and Constant Current (CC) outputs at two different sites with zero-phase frequencies, a dual-side LCC-LCC compensated WPT converter was thoroughly analyzed [5]. This analysis provided a systematic design strategy. Both weight and Compared to standard WPT topologies, this approach reduces bulk. By utilizing modern Analog Phase Control (APC) and Digital Phase Control (DPC) approaches, the method simplifies its control system by permitting CC and CV power transfer modes [6], [7]. To confirm the accuracy of this innovative method, a combination of simulation analysis and experimental data has been employed. Analyzing secondary active converters as a way to regulate power transfer in WPT systems shows that conventional WPT circuits usually use a front-end PFC interface, leading to large passive components that significantly impact system volume, losses, and dependability. Phase shifts between the primary and secondary sides occur because the primary side lacks intermediary storage elements. Typically, complex synchronization algorithms are used to calculate bridges [7]. For a Full-Bridge Active Rectifier (F-BAR) operating in Bidirectional

Wireless Power Transfer (BWPT), a new phase-shift control mechanism was developed. The traditional receiver-side rectifier design has to be altered as a result. Results from simulations and theory demonstrate how this novel control method allows output value control without requiring a transmitter-receiver connection. Maximum efficiency of 94.4% is attained with an output power range of 0 to 3.7 kW and an input voltage of 325V DC. The effectiveness of the converter and suggested control method is confirmed by the experimental validation. The paper's primary contributions include

ISSN: 2582-3930

- Dual-side phase shift-controlled methods enhance the power factor and regulate the power flow.
- The performance study of suggested techniques for the BWPT system, including frequency bifurcation, power loss, and THD.
- The dual side phase shift control method for the BWPT system was validated experimentally and through Modeling.

While Section III explores alternative BWPT control strategies, with a focus on phase shift control, Section II describes the various BWPT modes of operation. The bidirectional power flow control mechanisms between V2G and G2V are described in Section IV. A 3.7 kW system's design parameters and components are covered in detail in Section V, and an example for assessing the BWPT system's performance in both situations is given in Section VI.

The resonant converter incorporates PFC, with one strategy that was put into practice on the primary and secondary sides, respectively. The assessment mostly concentrates on important factors including efficiency, THD, and power losses.

II. WPT SYSTEM BIDIRECTIONAL

EVs are linked to the DC bus in the BWPT system through the WPT charging mechanism. Coupling coils, high-frequency converters, a compensation circuit, and controllers with specific designs make up each side of the system. The circuit diagram for the suggested topology is shown in Figures 2 and 3 under both charging and discharging circumstances. The primary converter functions as a DC/AC inverter when energy is transferred from the grid to the EV in G2V Mode, and the secondary converter acts as a regulated rectifier for AC/DC conversion. On the other hand, the converters' functions are inverted in V2G mode, when the EV battery feeds electricity to the grid [11]. The circuit consists of an

Volume: 09 Issue: 10 | Oct - 2025 SJIF Rating: 8.586 ISSN: 2582-3930

LCC-based resonant converter and a primary side inverter. a converter on the secondary side. In this bidirectional control design, regulation is achieved by matching the duty cycles of the inverters to modify the main side voltage (VP) or secondary end voltage (VS). Power regulation is made possible by varying the average low-frequency signal value of the primary side and secondary end voltages. As previously mentioned, the system consists of both primary and secondary compensation networks.

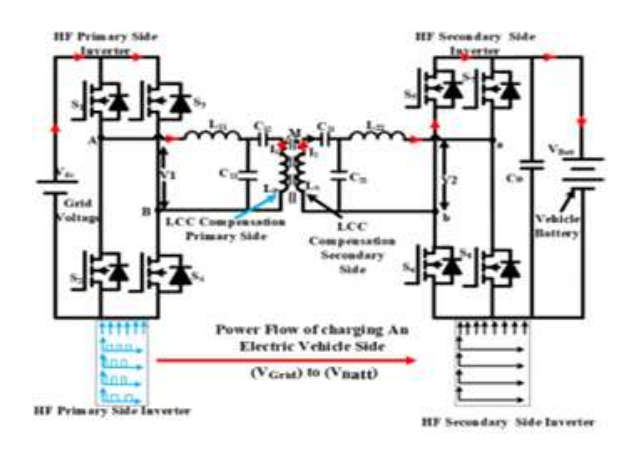


FIGURE 2. BWPT system for the Operation of (VGrid) Side to (VBatt) Side.

Through the use of mutual induction principles, which occur during the resonance situation, energy can be transferred from the primary coil to the secondary coil. The controllers play a critical function in overseeing the power transmission between the two coils through out each operational phase. An enhanced Pulse Width Modulation (PWM) approach is frequently used for phase shift control, in which control signals are sent to both sides of the converter switches. Fundamental techniques take into account the dual functionality of both primary and secondary converters when implementing bidirectional converters. When the battery receives power from the grid,

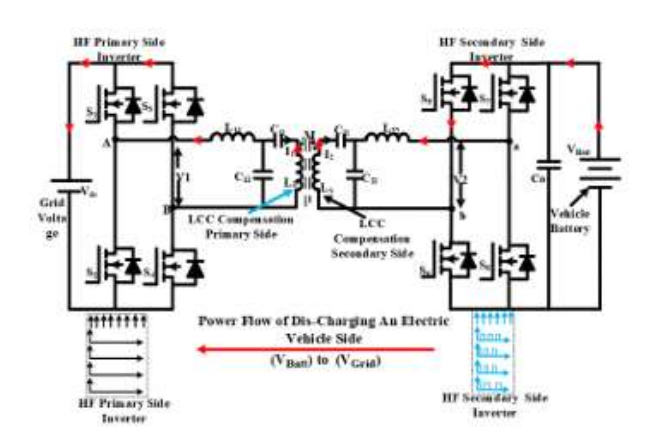


FIGURE 3. BWPT system for the Operation of (VBatt) Side to (VGrid) Side.

The primary converter is controlled by Phase Shifting Modulation (PSM) techniques, while the secondary side converter also serves as a rectifier at the same time. Figure 2 provides an example of this approach. Similarly, the AC/DC converter on the main side acts as a rectifier and the DC/AC converter on the secondary side as an inverter when electricity is transferred from the battery to the grid. Figure 3, which shows the discharge procedure, provides an illustration of this. This approach makes it simple to adjust the active power flow and calculates the expected efficiency. The power converters must cooperate in order to set up the settings in both controllers. By creating a wireless communication channel, this is accomplished without being constrained by signal processing latency. As a result, both controllers are easily synced and programmable.

A. BWPT OPERATION MODES Mode I: (α to π)

Switches S1 and S4 are conducting on the primary side during the time span αt to π , permitting current to flow through S1, the compensating inductance Lf1, the series and parallel capacitances C1, Cf1, and the primary coil L1. At the same time, this circuit also includes switches (S4). Switches S7 and S6 are operational at the same time on the secondary side. In order to reach the load, the induced current passes via the secondary coil (L2), compensating inductance (Lf2), series and parallel capacitances (C2, Cf2), and switches (S7) and (S6).

On the battery side of the car, the current moves forward across the load. The corresponding circuit of the bidirectional power transfer system described in Mode I is shown in Figure 4.

A. BWPT OPERATION MODES Mode I: (α to π)

Switches S1 and S4 are conducting on the primary



SJIF Rating: 8.586 ISSN: 2582-3930

side during the time span αt to π , permitting current to flow through S1, the compensating inductance Lf1, the series and parallel capacitances C1, Cf1, and the primary coil L1. At the same time, this circuit also includes switches (S4). Switches S7 and S6 are operational at the same time on the secondary side. In order to reach the load, the induced current passes via the secondary coil (L2), compensating inductance (Lf2), series and parallel capacitances (C2, Cf2), and switches (S7) and (S6). On the battery side of the car, the current moves forward across the load. The corresponding circuit of the bidirectional power transfer system described in Mode I is shown in Figure 4.

Mode II: $(0 \le t \le \alpha)$

The upper switches on the primary side, S1 and S3, are conducting across the time interval 0 to α . However, there is some dead time because the inductance's stored energy is released, which leads to a zero-current condition as the current flows between these two switches. Concurrently, during the same time period on the secondary side,

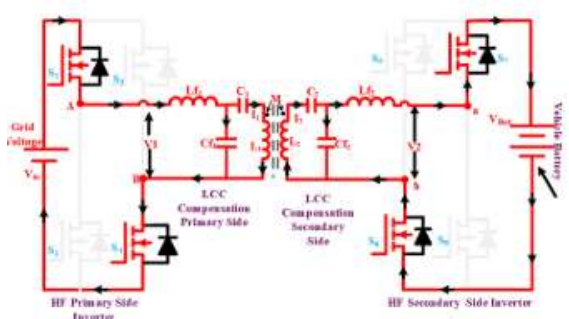


FIGURE 4. Equivalent circuit of presented BWPT operation in Mode I.

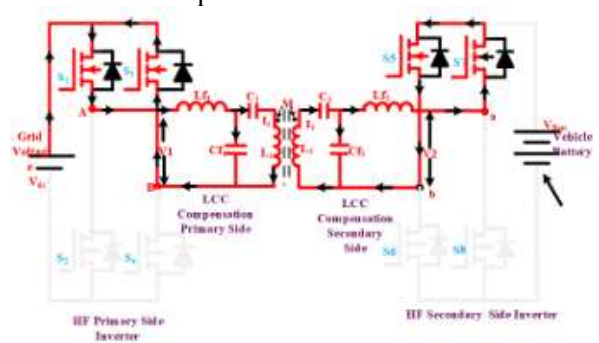


FIGURE 5. Equivalent circuit of presented BWPT operation in Mode II.

S5 and S7, the higher switches, are conducting. Like the primary side, there is a dead time during which current circulates between switches S5 and S7 as a result of the stored energy in the inductance. Consequently, there is no current flowing through the load [14]. An illustration of the equivalent circuit for the bidirectional power transfer system in operation during Mode II is shown in Figure 5.

Mode III: $(\pi + \alpha \le t \le 2\pi)$:

Switches (S2) and (S3) are operated on the primary side throughout the period ($\pi + \alpha t$ to 2π). Current (I) passes via the primary coil (L1), series and parallel capacitance (C1, Cf1), compensating inductance (Lf1), switches (S2), as well as the switches. At the same time, switches (S8) and (S5) are conducting on the secondary side.

The secondary coil (L2), compensating inductance (Lf2), series and parallel capacitances (C2, Cf2), switches (S8), load, and switches (S5) are all where the induced current passes.

On the vehicle's battery side, the current flows through the load in the opposite direction. The Mode III equivalent circuit operation is shown in Figure 6.

Mode IV: $(t \le \pi + \alpha \le \pi)$

The lower switches (S2) and (S4) on the primary side are conducting during the time interval (π to π + α).

Nevertheless, some dead time happens as a result of the inductance's stored energy being released, which causes current to circulate.

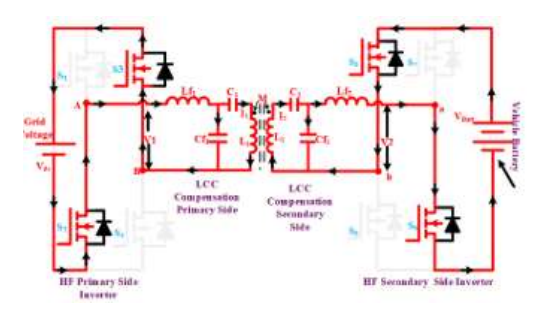


FIGURE 6. Equivalent circuit of presented BWPT operation in Mode III.

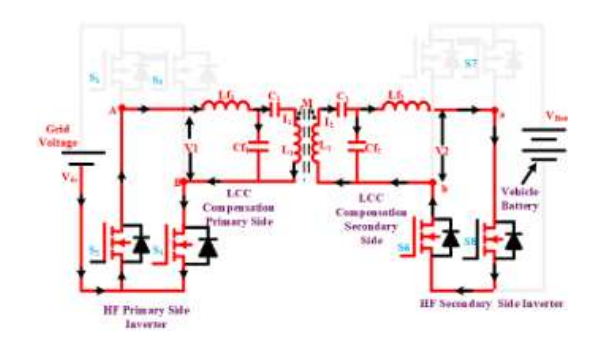


FIGURE 7. Equivalent circuit of presented BWPT operation in Mode IV.

Consequently, the current drops to zero between these two lower switches.

The two lower switches, S6 and S8, are conducting concurrently on the secondary side throughout the same time period. while with the primary side, there



SJIF Rating: 8.586 ISSN: 2582-3930

is a dead time while current flows between switches S5 and S7, respectively, as the inductance's stored energy is released. Consequently, there is no current flowing over the load. The analogous circuit for the bidirectional power transfer system in Mode IV is shown in Figure 7. Therefore, Figure 8 shows the switching waveforms for several bidirectional wireless power transfer techniques for V2G and G2V operations.

III. CONTROL OF PHASE SHIFT

For the primary side circuit to function at the secondary controller's rated current, the value α which depends on the reference signal—is essential. It is used to precisely modify the primary side inverter's output voltage. The phase shift (β) between the secondary inverter's legs simultaneously generated by the secondary controller, which affects the relationship between the primary and secondary output voltages. Lowlevel switching signals are used to implement the PWM approach, and these signals are then interpreted for the left and right sides by fine-tuning the phase shift parameters $(\alpha, \beta, \text{ and } \delta)$ [16]. In order to accomplish the

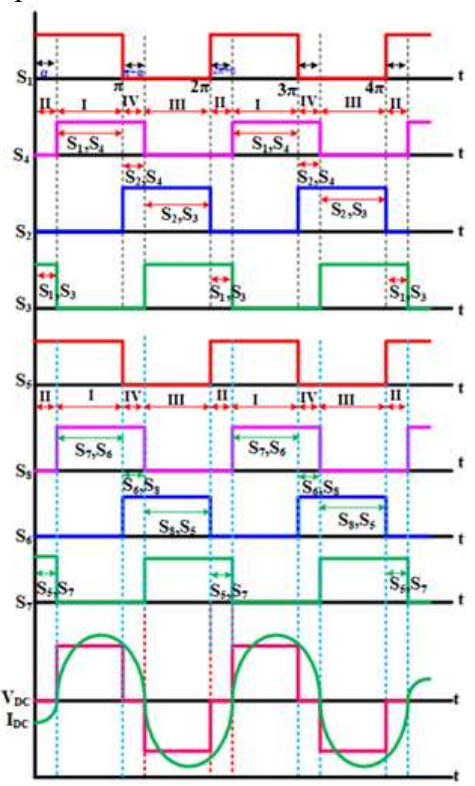


FIGURE 8. Switching waveforms of BWPT for V2G and G2V Operation.

The secondary side control parameters (β and δ) must be changed to achieve the appropriate power flow magnitude and direction. Signals amplified by the driving circuits determine the arrangement of the four switches on either side of the high-frequency

converters. These control parameters are essential for modifying the amplitude and phase of the inverter voltages as well as achieving the intended power flow throughout the system [17].

Every side in BWPT has the ability to act as a load and a supply at the same time. As a result, all parties need to be treated equally. There must be a deliberate lag in the activation of semiconductor switches on both ends in order to engage the fullbridge converters on the primary and secondary sides simultaneously. Phase angles (α, β) and the delay angle (δ) are used to control the power flow between the primary and secondary converters (AC/DC and DC/AC). The switching waveforms and the phase angle delay between the two converters are shown graphically in Figure 9. The power level is usually modulated on both sides by the phase shift angle. The phase difference between the primary and secondary inverters' peak voltages is indicated by the delay angle (δ) [18]. The two converters

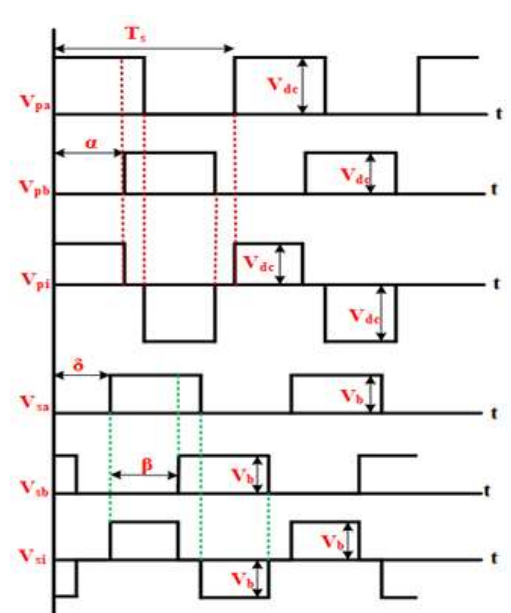
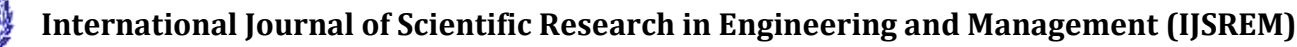


FIGURE9. Switching waveforms of phase angle delay between the two converters.

The output voltages for the first harmonics, VP(t) and VS(t), are written as

$$\begin{split} V_{p}(t) &= \left(\frac{4}{\pi}\right) V_{p} \sum_{n=1,3}^{\infty} \frac{1}{n} cos \left(n\omega_{r} t - \frac{n\alpha}{2}\right) sin \left(\frac{n\alpha}{2}\right) \\ V_{p}(t) &= \left(\frac{4}{\pi}\right) V_{p} \sum_{n=1,3}^{\infty} \frac{1}{n} cos \left(n\omega_{r} t - \frac{n\alpha}{2}\right) sin \left(\frac{n\beta}{2}\right) \\ (2) \end{split}$$

where the order of harmonics is denoted by n. In the equation above, α and β stand for the phase shift between an inverter pair's switches, VP and VS for





SIIF Rating: 8.586

current IP and IS.

provides more design alternatives for current rent and turn configurations than standard series compensation. Figure 2 displays the LCC-LCC compensating circuit layout of a linked coil. The following formula can be used to determine the

THEBWPTSYSTEM DESIGN IV. **PARAMETERS**

the primary and secondary side inverter peak

voltages, and "n" for the harmonic orders.

For the design of BWPT systems, the phase shift controller with enhanced PFC control must be developed. At the resonance frequency, the power transfer between the primary and secondary coils can be stated.

$$P = \omega 0 M I_p I_s \tag{3}$$

This example shows the mutual inductance between the primary and secondary coils. The letters IP and IS stand for the Root-Mean-Square (RMS) current flowing through the primary and secondary coils, respectively. The mutual inductance between these coils is essential in wireless charging systems since it directly influences the effectiveness and power transfer efficiency. The operating frequency of 85 kHz in this specific situation is in line with the SAEJ2954 standard. The expression for the output power is then as follows:

$$p = 2\pi f 0(N_P I_p)(N_s I_s) K \sqrt{\hat{L}_p \hat{L}_s}$$
 (4)

where the operating frequency is denoted by f0. The letters NP and NS stand for main and secondary coil turns, respectively. The inductance return is represented by the symbols ^ LP and ^ LS for the primary and secondary coils, respectively.

K is a representation of the coupling coefficient between the coils. There will be a smaller air gap if Kislow, and vice versa. The equations determine the mutual inductance per return based on the size and air gap between the charging pads.

$$M = K\sqrt{L_p * L_s} \tag{5}$$

Larger pad diameters and a smaller air gap lead to an increase in mutual inductance (M) [20]. The coupling coefficient (K) rises by 30% to 50% because the ferrite core's self-inductance is almost double that of the air core. [21]. To guarantee that the receiver and transmitter pads are the same size, it is crucial to regulate the output power and ampereturn ratio. The dimensions of the charging coil and the airgapto were used to generate a 3D finiteelement analysis (FEA) model with an alumped coil, which computed the coupling coefficient and inductance return. The ampere-turn architecture of the primary and secondary side coils is still an important design factor for the given size, power rating, and air gap [22]. The LCC compensation

$$IP = \frac{V_{AB}}{\omega_0 L_{11}}, I_S = \frac{V_{ab}}{\omega_0 L_{22}} \tag{6}$$

According to equation (6), the compensatory inductances L11 and L22 have an impact on the currents IP and IS for the voltage at input-output. A decrease in the coil current IP is made possible by a change in the value of the compensating inductance L11. With LCC-LCC compensation, several coil current ranges (IP) for a given voltage may be found, and the number of turns (NP) can be defined [23]. When an excessive number of turns is chosen to minimize a coil's current, the coil's inductance and the voltage across it notably increase. An very high voltage may raise security and reliability issues due to the insulating layer and turn-to-turn distance of the Litzwire. Furthermore, the maximum voltage of the system may be restricted by certain applications. As a result, the voltage across the coils and capacitor limits the number of spins; equations (7) and (8) can be used to quantitatively depict this relationship.

$$V_{LP} = I_{P}X_{LP} = j\omega L_{P}I_{P} = I_{P}(2\pi N_{p}^{2}\hat{L}_{p}) (7)$$

$$V_{LS} = I_{S}X_{LS} = j\omega L_{S}I_{S} = I_{S}(2\pi N_{p}^{2}\hat{L}_{p}) (8)$$

The voltage across the coils rises by $[2\pi IpNp^{\hat{}} LP]$ for each consecutive rotation, per the equation above. The following formula is used to determine

the input voltage to coil voltage ratio:
$$G_{Vp} = \frac{V_{LP}}{V_{AB}} = \frac{X_{LP}}{XL11} = \frac{L_P}{L11}$$
(9)

By estimating the resonance frequency, capacitor value for LCC-LCC correction can be ascertained following coil design and inducer

canoration:

$$\omega_0 = \frac{1}{\sqrt{L_{11}C_{11}}} = \frac{1}{\sqrt{(L_P - L_{11})C_{12}}}$$

$$\omega_0 = \frac{1}{\sqrt{L_{22}C_{22}}} = \frac{1}{\sqrt{(L_S - L_{22})C_{21}}}$$
(11)

$$\omega_0 = \frac{1}{\sqrt{L_{22}C_{22}}} = \frac{1}{\sqrt{(L_S - L22)C21}} \tag{11}$$

Similarly, the pad's design is based on three key elements: the width of the ferrite core to prevent excessive core loss, the number of turns per coil to accomplish the required self-inductance, and the current rating of each coil, all of which contribute to the Liitzwire gauge. To achieve the standards for capacitor voltage and inductor current, a thorough analysis of electrical, magnetic, and thermal

Page 7

© 2025, IJSREM | https://ijsrem.com DOI: 10.55041/IJSREM53336



SIIF Rating: 8.586

properties is necessary [24]. Use equations (12,13) to depict the currents flowing through the tuning inducers and primary and secondary coils of an LCC-LCC resonant tank.

$$IL_{11} = \frac{MV_{AB}}{\omega_0 L_{11} L_{22}}, L_{22} = \frac{MV_{ab}}{\omega_0 L_{11} L_{22}}$$
(12)

$$IL_{11} = \frac{MV_{AB}}{\omega_0 L_{11}}, L_{LS} = \frac{V_{ab}}{\omega_0 L_{22}}$$
(13)

$$IL_{11} = \frac{MV_{AB}}{\omega_0 L_{11}}, L_{LS} = \frac{V_{ab}}{\omega_0 L_{22}}$$
 (13)

The voltage ages between the tuning capacitors in LCC-LCC resonance-compensated systems can be computed using equations (14)–(15).

$$V_{C12} = \frac{V_{AB}(L_P - L_{11})}{L11}$$

$$V_{C21} = \frac{V_{AB}(L_S - L_{22})}{L22}$$
(14)

Furthermore, the high-frequency high-power capacitor must meet both the voltage and current requirements while taking into account the heating constraints. The actual rated voltages and currents for the proposed design's resotank components are shown in Table 1.

V. Correction of the **Power Factor INTHEBWPTSYSTEM**

Power Factor Correction (PFC) can be implemented at the front-end or back-end of an ideal WPT system. But it's important to keep in mind that choosing between front-end and back-end PFC depends on a number of variables, such as system efficiency considerations, and design constraints [25]. Every strategy has pros and cons of its own, and the choice should be based on the particular requirements of the system. In a perfect WPT

TABLE1. Electrical circuit parameters of 3.7 KWBWPT system.

1			•
S: No	Parameters	Symbols	Values
1	Output Power	P_{out}	3.7 kW
2	Input AC voltage	V_{Grid}	325 V
3	Output Converter Voltage	V_{out}	420 V
4	Coupling Co-efficient	K	0.4
5	Switching Frequency	f_s	85 kHz
6	Mutual Inductance	M	46.5µH
7	Capacitor for Primary Side Series Compensation	C_p	31nF
8	Self-Inductance of the Primary Coil	$\mathbf{L}_{\mathbf{P}}$	120 μΗ
9	Secondary Coil Self Inductance	L_{S}	120 μΗ
10	Secondary Side Series Compensation Capacitor	C_8	31nF
11	Capacitance Filter	C_0	30 μF

system, the following is an expression for power transmission at the resonance frequency:

$$P_o = \frac{8}{\pi^2} * \frac{V_P * V_S}{\omega * L_M} \tag{16}$$

The interaction between self and mutual inductance can be calculated using the LM, which is calculated using the coupling factor value, the distance between the primary and secondary coils, and the coil misalignment. The letters LP and LS represent the respective self-inductance of the primary and secondary coils. The Kvalue fluctuates primarily in the range of 0.2 to 0.5. The output power can be adjusted using either VP or VS, and the resonance frequency is independent of the load. The automobile SAE standard J2954 describes a frequency spectrum that ranges from 81.39 kHz to 90 kHz. The PFC model includes compensation coupled to an H-bridge converter on both the main and secondary sides, as well as active rectification. Furthermore, the output interfaces for battery charge control have passive DC-DC control. It is believed that power in single-phase alternating current (AC) systems is proportional to the quadratically-sine function, assuming that the unity power factor is corrected.

ISSN: 2582-3930

$$P_g(t) = 2V_g I_g sin(\omega_g t)$$
 (17)

where Vg and Ig stand for the grid's input voltage and RMS current, respectively. The switching frequency is not a control variable in this scenario. Therefore, controlling the average low-frequency primary voltage (Vpf) or secondary voltage (Vsf) is how power regulation is achieved. This allows for a 100Hz variable power source while guaranteeing PFC. Thus, the power transfer can be computed as

$$P_g(t) = V_g I_g = P_{mean}(1 + cos(2\omega_g))$$
(18)

This study makes the assumption that continuous current (CC) and continuous voltage (CV) control cooperate to regulate batteries. We'll use battery current and voltage readings to operate this control mechanism. In order to assist with CC management, Additionally, a current saturation mechanism has been incorporated. The internal current control loop, which effectively counteracts both internal and external disturbances, becomes essential to the regulation of the accurate current. The transmitted power can be calculated as follows since the secondary-side voltage and the resonant current are always in line.

$$p = \frac{p_{mean}^* M \omega_0 \pi}{2V_{BAT}} = \frac{4}{\pi \omega_0 i \hat{P}}$$
 (19)



International Journal of Scientific Research in Engineering and Management (IJSREM)

Volume: 09 Issue: 10 | Oct - 2025

SJIF Rating: 8.586

ISSN: 2582-3930

where ^ Vpf and ^ Vsf, respectively, represent the fundamental voltage amplitudes on the main and secondary sides at the switching frequency.

$$v_{\widehat{Pf} = \frac{4}{\pi} V_r \sin(\delta_P \pi/2)} \tag{20}$$

$$v_{\widehat{Pf} = \frac{4}{\pi} V_{BAT} \sin(\delta_P \pi/2)} \tag{21}$$

where the primary and secondary duty cycles are denoted by δp and δs , respectively. VBAT is the battery voltage, and Vr is the rectified grid voltage. Both PFC control techniques require a grid-connected unfolding 50 Hz active rectifier, regardless of the converter that performs PFC and current shaping.

By adjusting unregulated (AC) voltage, resonant inverters regulate the primary resonant tank (VP) and the current flow between the primary and secondary coils. Furthermore, when an off-board primary-side resonant inverter manages the power control, communication systems or estimate techniques are required.

A. THE FIRST SIDE PSM Management

In order to regulate the battery charging process, primary-side control (PSC) alters the primary voltage (VP); the secondary voltage (VS) remains uncontrolled. Phase-Shift Modulation (PSM) is used in the primary-side resonant inverter as part of a duty-cycle management strategy to accomplish this. All switches in this configuration are square modulated, and the duty cycle (δp) is controlled by the phase difference between the two inverter branches. There are two operational options available to lower conduction losses on the secondary side: synchronization with the resonance current or a passive converter. It is feasible to produce a primary current with a constant amplitude in both situations. The duty-cycle calculation method is the same for both operation modes, with the pulse generation approach serving as the main of differentiation. Additionally, operational frequency of each switching device either the line frequency or the switching frequency—may affect the pulse patterns. It is expected that the primary coil current maintains a sinusoidal waveform with a constant amplitude in both G2V and V2G operations. It is therefore necessary to manage the primary voltage in order to modulate fluctuating power. The primary voltage can be used to determine the variable power. Equations (20) and (21) allow us to define the fundamental voltage reference in the following way: $V_p^{\wedge *}V_p^*(1+\cos(2\omega_g))$

where, in the following equation, V* p value is substituted,

$$V_p^{\wedge *} = \frac{p_{mean}^* M \omega_0 \pi}{2 V_{BAT}} (1 + cos(2\omega_g)$$
 (23)

The previous equation (23) [22] can be used to derive the cosine waveform for the grid measuring system with Phase-Locked Loop (PLL) synchronization. In a similar manner, peak current measurement at the primary coil yields the Magnitude to Voltage of the Battery Voltage (M/(VBAT)) (24).

$$\frac{M}{V_{ABT}} = \frac{4}{\pi \omega_0 i_p^{\wedge}} \tag{24}$$

Since the limits of both parameters are somewhat large and alternative methods are needed for an accurate VBAT estimation, it is difficult to extract M and VBAT separately from the primary side's steady-state data. The duty cycle expression for the primary side can be computed using equation (20) as follows.

$$\delta_P = \frac{2}{\pi} \alpha sin\left(\frac{\pi V_p^{\wedge *}}{4_{vr}}\right) \tag{25}$$

B. THE SECONDARY SIDE PSM MANAGEMENT

In the secondary-side control technique, a Phase Shifted Pulse-Width Modulation (\deltas) regulates the secondary rectifier's duty cycle (PWM). By altering the secondary side's voltage, an unconstrained square-wave modulation can generate a primary current with a variable amplitude. In the event that the on-board system fails, the secondary coil current can be used for the PLL input to measure grid voltage. In any case, these secondary voltage references must fulfill the following specifications:

$$v_s^{\wedge *} = V_s^{\wedge} [sin(\omega_g t)] = \frac{p_{mean}^* M \omega_0 \pi}{2V_{BAT}} [sin(\omega_g t)]$$
(26)

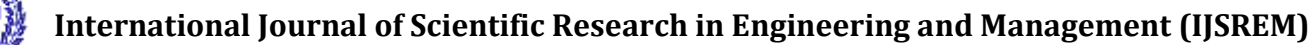
The secondary peak current values can be used to estimate the M/Vgrid value because it is challenging to get these variables separately (24). In this instance, the coupling factor can be estimated using a comparatively small range of grid voltage amplitude.

$$\frac{M}{v_r} = \frac{4}{\pi \omega 0 i_s^{\wedge}} \tag{27}$$

We may determine the duty cycle from the secondary side by integrating with equation (6) and using the following equation:

$$\delta_P = \frac{2}{\pi} \alpha sin\left(\frac{\pi V_p^{\wedge *}}{4V_{BAT}}\right) \tag{28}$$

Additionally, the pulse patterns of each switching device are supplied and distinguished between switches that work at line frequency and those that serve as switching frequency fs [24], [25].



SJIF Rating: 8.586

ISSN: 2582-3930

C. INVERTER PHASE SHIFT PWM TECHNIQUES

Because of their exceptional efficiency, low levels of electromagnetic interference (EMI), and lack of voltage fluctuation issues, phase-shift control works well for H-bridge converters. The PSM is often constructed as follows when the angular switching frequency of the converter is aligned with the angular resonance frequency of the resonant tank:

$$\omega_0 = \frac{1}{\sqrt{L_1 C_1}} = \frac{1}{\sqrt{L_2 C_2}} \tag{29}$$

Inverter technology exploration: the switches (SP1-SP4) and (SS1-SS4) represent the switches on both the primary and secondary sides, as well as the control signals that go with them. The control signal is the internal phase-shift angles (α, β) of the primary and secondary sides, which regulate the time interval to match the DC-link voltage. A sufficient control over the power transfer can be achieved by adjusting the phase delay (ϕ) of the primary and secondary control signals. The two independent controllers cannot be started simultaneously due to the unpredictable wireless communication delay and clock discrepancies between them. The delay assumes the properties of an unknown phase delay due to the erratic directions for start. The distance between the primary voltage (VP) and secondary voltage (VS) center points is represented by the relative phase shift angle (γ) . This equation shows how $(\alpha, \beta, \text{ and } \gamma)$ are related to each other.

$$\gamma = \varphi + \varphi_{delay} - \frac{\alpha}{2} + \frac{\beta}{2}$$
 (30)

The equation above illustrates how the internal phase-shift angles of the primary and secondary sides (α, β) affect the relative phase-shift angle (γ) . Changing (γ) can efficiently direct the power transmission of the BWPT system, and changing α and β can control it. With respect to the clock pulse, the PWM signal produced by the principal side controller for the switches (SP1–SP3) has a leading (lagging) angle of $\alpha/2$. phase The delayangle (ϕ) between the primary and secondary controller clocks is employed for the secondary controller's adjustable angle. The control signal for the switch (SS1-SS3) is generated using the phase angle of $(\phi + \beta/2)$ and $(\phi-\beta/2)$ in order to regulate the secondary side. Therefore, converters' primary and secondary side control signals with corresponding phase-shift angle fluctuations are shown as

$$\gamma = \varphi_{delav} + \gamma \tag{31}$$

The charging mode's value of (γ) is set to $\pi/2$, while the discharging mode's value is set to $3\pi/2$ in order to maximize power transfer efficiency for the BWPT system. It is simple to accomplish this modification by controlling (φ) . The direction and amplitude of the system's transfer power can be changed by adjusting this variable. Additionally, the relationship between the quantity of transfer power, the dead-time effect, and the internal phase-shift angles must be taken into account. The values that need to be computed in order to obtain the required transfer power become crucial in this situation.

D. BIFURCTION

Bifurcation problems are covered in great detail in the literature, and designers usually try to avoid this issue by considering operating conditions when designing coils and resonant correction. Bifurcation should be prevented by taking into account a number of factors, such as the compensating capacitor, transmitted power, coupling factor, and the ratio of coil self-inductances. The capacity of a system to operate in both directions may limit the possibility of avoiding specific issues, depending on the system's specific requirements. Figure 10 shows how well the BWPT system works when using suggested control measures. demonstrating how the switching frequency and coupling factor (k) affect system performance. This resonant inverter exhibits the capacity to function in a number of zones, requiring hard switching, such as inductive, Zero Voltage Switching (ZVS), and Zero Current Switching (ZCS). Depending on the frequencydependent load impedance, bifurcation is essential in identifying the resonant inverter's switching modes. The bifurcation point therefore has a major influence on system performance, especially with regard to power losses in semiconductors, which in turn has a major effect on system efficiency.

© 2025, IJSREM | https://ijsrem.com

SJIF Rating: 8.586

Volume: 09 Issue: 10 | Oct - 2025

600 A B C D 5 qq

FIGURE 10. Operating points of the wireless charger.

time(h)

Consequently, the following can be used to identify the proposed system's bifurcation limits:

$$P_{Limt} = \frac{V_s^2}{2\omega 0 L_s P} \qquad K \tag{32}$$

$$K_{Limt} = \frac{\tilde{V}_s^2}{2\omega 0 L_s P} \tag{33}$$

$$x_{limit} = \frac{\hat{v}_p}{\hat{v}_s} \tag{34}$$

where the coil inductance ratio, denoted by x, is

$$x = \frac{L_p}{L_s} \tag{35}$$

By extending the input impedance expression, the bifurcation is analyzed for G2V operation.

The following formula can be used to determine the load resistance AC value from the secondary side:

$$Z_{in} = \frac{\vec{V}_p}{\vec{\iota}_p} \tag{36}$$

When the primary side controller is implemented as follows, its resistance is determined by the output equivalent resistance:

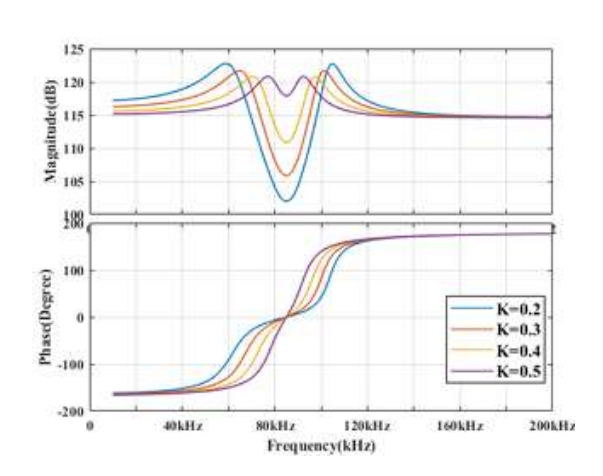
$$R_{SAC} = \frac{v\hat{s}}{i\hat{s}} \tag{37}$$

The output equivalent resistance determines the resistance of the primary side controller when it is implemented as follows:

$$R_{SAC} = \frac{\frac{4}{\pi}V_{BAT}}{\frac{\pi}{2}i_{BAT}} = \frac{8}{\pi^2}R_{2,DC}$$
(38)

Conversely, when using the secondary control technique, the associated AC resistance changes with the duty cycle [24].

$$R_{SAC} = \frac{8}{\pi^2} R_{2,DC} sin^2 \left(\frac{\delta_S \pi}{2} \right)$$
 (39)



ISSN: 2582-3930

FIGURE 11. Bode diagram illustrating the input impedance (Zin) for various coupling factors (k) with primary control.

The input impedance is described as follows at a specific resonance instance:

$$Z_{in} = \frac{\omega_0^2 k^2 L_p L_s}{R_{SAC}} \tag{40}$$

Figure 10 displays a bode diagram that plots the input impedance magnitude against the switching frequency. A positive phase indicates inductive activity, which makes Zero Voltage Switching (ZVS) possible [26]. However, because a capacitive zone coincides with a negative phase, hard-switching is necessary. Even when there are significant bifurcation problems, primary-side control remains unaffected by them, according to an analysis of it.

values of the coupling factor, as seen in Figure 11. However, as Figure 12 illustrates, bifurcation problems with secondary-side control occur when working with large coupling factors (k > 0.3).

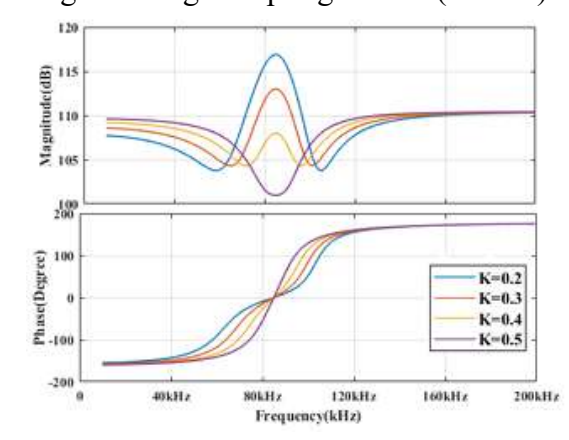
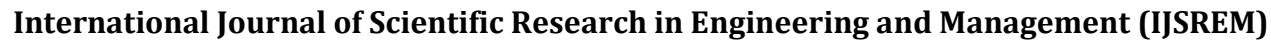


FIGURE 12. Bode diagram illustrating the input impedance (Zin) for various coupling factors (k) with secondary control.

The secondary-side control exhibits bifurcation when the coupling factor is high, whereas the





SJIF Rating: 8.586

primary-side control does not, even at high coupling factors. Furthermore, the bifurcation is investigated for a variety of coupling coefficient values, from K=0.2 to K=0.5.

The power, coupling, and voltage ratios are close to the bifurcation limit for k=0.2. Since the secondary voltage is higher than the main voltage and the power and coupling are both below the allowed limits, there is no bifurcation when K=0.3. There is no bifurcation for K=0.4 & 0.5, respectively, since the power and coupling are both above the the secondary voltage is lower than the primary voltage and is within the necessary limits. The frequency is split into two parts, a higher angular frequency (ωH) and a lower angular frequency (ωL), as the coupling coefficient rises above the critical coupling value. Both frequencies combine and the phase angle is zero when the coupling coefficient equals the critical coupling coefficient (KC). Both phase angle frequencies are eliminated by further lowering the coupling coefficient. For best gain and bifurcationfree operation, the coupling coefficient must be smaller than the critical coupling coefficient.

E. PFC CONTROL AND THD

The resonant circuit is used to operate near the resonant frequency but with minimal outside the point to maintain the inductive energy in the circuit in order to achieve the ZVS operation of the inverter. However, sufficient induced voltage must be maintained at the secondary coil for the BWPT systems to maintain a constant output. The difference between controlled and unrestricted output voltage functioning is what makes the difference. When the frequency of switching is not exactly in resonance and does not produce

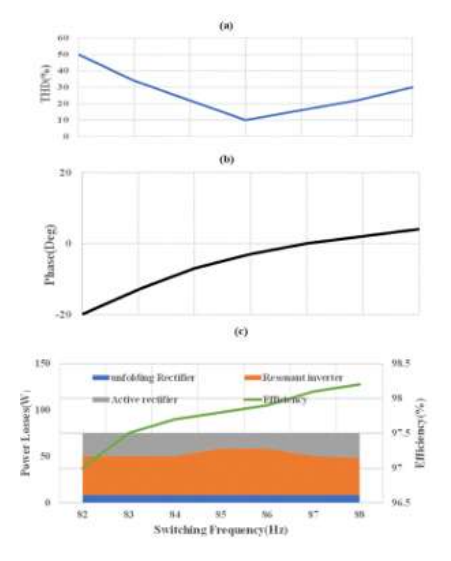


FIGURE 13. Primary-side control strategy effectiveness about coupling factor and switching frequency a) Input current THD b) Phase angle at Primary side c)

Efficiency and Power loss.

ISSN: 2582-3930

The secondary rectifier may behave nonlinearly if there is sufficient voltage to bias the semiconductor components. When using two control approaches, this nonlinearity affects the input current Total Harmonic Distortion (THD) and is caused by the minimal induced voltage. This becomes particularly important in low-load situations, such the final segment of continuous voltage at the D point, or when grid voltage zero-crosses. In the vicinity of the grid zero crossing, the principal control method is unable to produce enough voltage. As a result, there is no active power transfer and the current flows nonlinearly, which results in insufficient PFC. But the THD characteristic is When primary-side control is used, tics show notable increases in the resonance frequency. Figure 13. shows that there is a discernible improvement in Total Harmonic Distortion (THD) when the switching frequency is changed. This enhancement is ascribed to the reduction of the resonant tank's voltage drop, which raises the induced voltage. On the other hand, secondary control is less affected by resonance deviations, resulting in a comparatively low THD over the frequency range examined in Figure 14. Consequently, primary control functions without experiencing bifurcation, which helps to enhanced effectiveness, especially at frequencies higher than resonance. Zero Voltage Switching (ZVS) and the resulting reduction in inverter power losses are credited with increasing efficiency. On the other hand, secondary-side control undergoes bifurcation, which produces improved efficiency an characteristic below the resonance frequency.

SJIF Rating: 8.586

Volume: 09 Issue: 10 | Oct - 2025

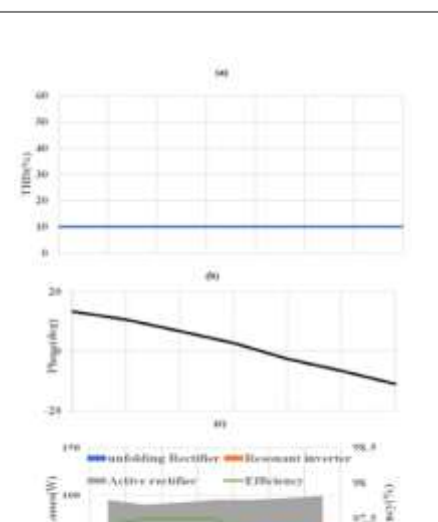


FIGURE 14. Secondary-side control strategy effectiveness about coupling factor and switching frequency a) Input current THD b) Phase angle at Primary side c) Efficiency and Power loss.

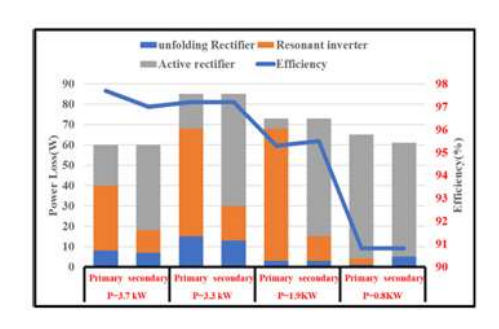
F. LOSS OF POWER

A thorough investigation of the various system components and the corresponding power losses are necessary to assess the BWPT system's performance in both G2V and V2G modes. The main loss taken into account in the evaluation is the semiconductor switching loss that happens at each stage of the power conversion. Furthermore, switching losses are added to the secondary rectifier by the carrier signal that is in phase with the secondary's current. Additionally, the frequency bifurcation is reduced when the switching frequency is chosen close to the resonant frequency. Equation (41) displays the overall system efficiency, which is the ratio of the system's basic equation pertaining to output power to input power.

$$\eta_{total} = \eta_{rectfier} \times \eta_{HFPC} \times \eta_{compensation} \times \\
\eta_{pad} \times \eta_{compensation} \times \eta_{HFPC} \times \\
\eta_{Bidirectional(DC-DC)} = \frac{P_{output}}{P_{input}} = \frac{P_{input} - P_{plosses}}{P_{input}} \\
(41)$$

The sum of the front-end converter (FEC), high-frequency primary converter (HFPC), charging pad (CP), compensation networks (CN), high-frequency secondary converters (HFSC), and the

$$p_{loss} = P_{1-rectifer} + P_{1compensation} + p_{l-pad} + P_{l-compensation} + P_{l} - HFSC + P_{l-Bidirectional(DC-DC)} converters$$
 (42)



ISSN: 2582-3930

FIGURE 15. The power loss and efficiency performance at different operating points at 85 kHz and k=0.2.

The rated voltage and current from, angular frequency (ω), inductance (L), and windings of the AC resistance coils from (43) can all be used to determine the charging pad losses.

$$p_{l-copuler} = P_{l-winding} + P_{l-core}$$
(43)

Equation (44) provides the power losses across the charging pads.

$$P_{l-coupler} = (I_{mis}^2 \times r_{ac}) + (C_m \times f_{sw}^{\alpha} \times \beta^{\beta})$$
(44)

The core loss of the charging pad can be determined using the Steinmetz equation, taking into account the values of the coupling coefficient, flux density (B), and system frequency (fs). By estimating the switching and conduction losses of the operating SIC MOSFET, the inverter's losses may be computed. Likewise, the sum of these losses might be used to calculate the diode's losses.

$$P_{l-MOSFET} = P_{l-conduction} + P_{l-switching} + P_{l-driving} = (R_{ds}(on) \times I_{ms,M}^{2}) + V_{DS} \times I_{rms,M} \times t_{on,M} + (V_{DS} \times I_{M} \times t_{off,M})) \times f_{sw} + (2 \times g_{s} \times q_{as})$$

$$(45)$$

$$P_{l-MOSFET} = P_{l-conduction} + P_{l-switching} = V_F \times I_{avg.D} + R_d \times I_{rms.D}^2) + (Q_{rr} \times V_{diode}) \times f_{sw}$$

$$(46)$$

Equation (45) indicates that the commutation voltage is represented by VDS, the MOSFET switches' on-state resistance is represented by Rds,ON, and the current passing through the switches is represented by I2 rms, M, and Vgs and Qgs represent the gate-to-source terminal

voltage and charge. VD stands for the diode voltage, and VF for the forward voltage. The average (42)

© 2025, IJSREM | https://ijsrem.com



International Journal of Scientific Research in Engineering and Management (IJSREM)

Volume: 09 Issue: 10 | Oct - 2025

SJIF Rating: 8.586

(43) (44) (46) and rms current values of the diode are denoted by Iavg,D and I2 rms,D, respectively. ZVS claims that in order to reduce inverter power losses, the primary control functions without bifurcation produce higher efficiency above resonance frequency. Furthermore, bifurcation is shown by the secondary side control, which leads to better efficiency characteristics below the resonance frequency. Similar to the major side control method, obtaining ZVS in unbifurcated systems is rather simple because the load's input impedance is always inductive above resonance frequency. A thorough rundown of the system's overall Figure 15 shows the power losses and performance at each level. Only the power losses that semiconductor devices encounter are taken into consideration in these calculations. As was previously said, the carrier signal that is in phase with the secondary's current also causes the secondary rectifier to experience switching losses. Additionally, the frequency bifurcation at the secondary-side control is reduced when the switching frequency is chosen close to the resonant frequency. The efficiency results indicate that both control systems have equal overall power losses, despite differences in the distribution of

VI. OUTCOMES AND TALK

these losses.

According to the specifications listed in Table 1, a simulation analysis and experimental verifications are conducted for the proposed system's 3.7 kW power rating. For both the G2V and V2G modes of operation, the MATLAB simulation is run. Important characteristics are measured, including the grid side voltage and current, the transmitter and reception coil sides, and the inverter end. The output voltage at the secondary inverter side (Vout) is 420V, and the input AC voltage (VGrid) is 325V. These simulation settings are in accordance with the guidelines provided. Consideration is given to an 85 kHz switching frequency (fs) and a coupling coefficient (K) of 0.4. The parts of the system include of the subsequent parts: the primary coil's self-inductance (LP), the secondary coil's selfinductance (LS), the secondary side series compensation capacitor (CS), the capacitance filter (C0), and the primary side series compensation capacitor (CP). It is believed that the mutual inductance (M) is 46.5 µH. This comprehensive simulation study ensures a thorough analysis of the performance of the proposed dual-phase shift Pulse Width Modulation (PWM) technique under varied

operating circumstances.

A. G2V SIDE SIMULATION RESULTS

First, the G2V operational simulation mode is used, taking into account a grid frequency of 50 Hz and a grid supply voltage magnitude of 325V. The nominal grid input voltages' sinusoidal change is depicted in Figure 16(a). The voltage and current of the primary side converter are shown in

ISSN: 2582-3930

The waveform in Figure 16(b) shows that the THD is lower when operating in the G2V mode with primary side control. On the other hand, the voltage and primary coil current plotted

Figure 16(c) and (d) demonstrate that voltage harmonics are present.

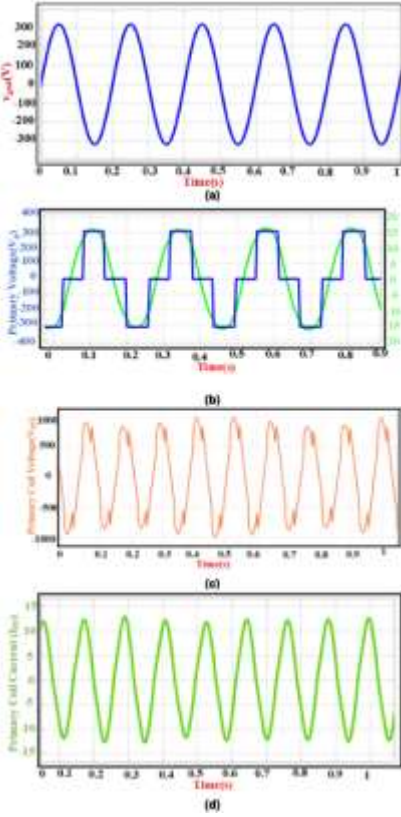


FIGURE 16. (a) The Grid Input Voltage (b) Primary side Converter voltage control (Vpp) Current (Ipp) (c) Primary coil voltage (Vpp) across the transmitter pads (Vpp) (d) The Primary coil current across the transmitter pads (Ipp).

On the other hand, the modulated current (Ipp) is 12A and the modulated voltage (Vpp) is nearly 940 V on the primary coil side. On the other hand, Figure 17(a) displays the secondary side voltage and current, which are 220V and 18A, respectively, due to unregulated secondary side regulation. In the same way, the secondary coil side modulated current (Iss) is 8 A, and the secondary coil side modulated voltage (Vss) is 1000V. The secondary side waveform shows that there are more voltage harmonics present than current.

SJIF Rating: 8.586

FIGURE 17. (a) Secondary side Converters voltage control (Vss) Current (Iss) Waveforms (b) Secondary coil voltage (Vss) across the Receiver pads (c) Secondary coil Current (Iss) across the Receiver pads.

the coil end's harmonic level. Additionally, the compensating resonance capacitance at the secondary converter's output reduces the THD level.

The primary side control offers superior control over the THD and bifurcation at the primary and secondary ends, according to the simulation research results for the G2V operation. Conversely, the same PFC is brought about during G2V operation by the utilization of unregulated operation at the secondary side.

When using the V2G operation for secondary control, the improvement in the PFC was visible.

B. V2G SIDE SIMULATION RESULTS

The secondary converter is controlled during the V2G portion of the simulation research, and the primary side converter is not modulated. With the exception of the control flow modifications, the design parameters are the same for the G2V operation. The voltage and current of the primary side unregulated square-wave modulation converter are displayed in Figure 18(a). The principal current (Ipp) and primary side voltage (Vpp) have peak values of 10 A and 150 V, respectively. In the meantime, the sinusoidal current is displayed in Figures 18(b) and 18(c) and fluctuating voltage that comes from the voltage and current of the primary side pad. In comparison to the voltage, the primary side has the lowest current THD. Additionally, in

V2G mode of operation, the PFC at the main side with secondary end control is improved. fluctuating voltage that comes from the voltage and current of the primary side pad. In comparison to the voltage, the primary side has the lowest current THD. Additionally, in V2G mode of operation, the PFC at the main side with secondary end control is improved.

ISSN: 2582-3930

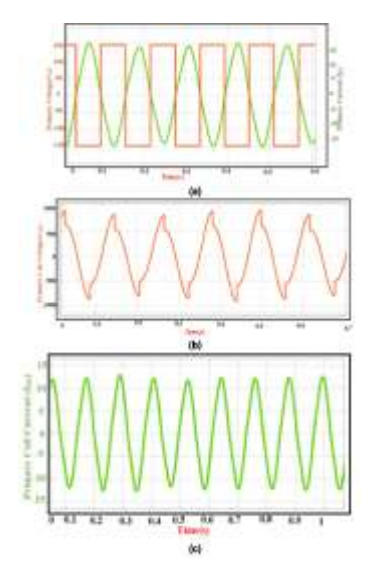
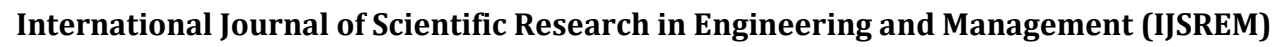


Fig. 18. Current (Ipp) at the primary side, converter voltage (Vpp), voltage (Vpp) across the primary pads, and primary coil current (Ipp) are the first three variables. Figure 19(a) through 19(c) show the side parameters. secondary measured secondary side converter voltage and current, with amplitudes of 310 V and 8 A, are displayed in Figure 19(a). Likewise, Figure 19(b) and Figure 19(c) show the secondary side coil voltage and current. The coil's voltage and current are 600V and 8A, respectively. The enhanced PFC over the primary side control is demonstrated by the secondary side control operating in the V2G mode. In contrast, the bifurcation and THD remain unaltered in V2G mode.

VII. ANALYZATION

The suggested work provides an appropriate method for addressing issues that come up in BWPT systems used for EV charging. The proposed dual-phase shift-regulated PWM methodology offers an advanced power factor control strategy intended for two-way operations, surpassing the limitations of conventional power factor control techniques. To support the efficacy of the suggested system, a comprehensive study is carried out, accounting for elements including power factor, bifurcation, total



IJSREM e Journal

Volume: 09 Issue: 10 | Oct - 2025

SJIF Rating: 8.586

harmonic distortion (THD), and power losses. Simulation and experimental validation evaluations for G2V and V2G modes show power transfer efficiencies of 94.4% and 90.1%, respectively, for a 3.7 kW power rating at an operating frequency of 85 kHz. The mode of V2G of operation with dual phase shift control provides improved power factor management without altering the bifurcation factor and THD. On the other hand, the THD and bifurcation are improved by the G2V mode of operation with the primary control. This study highlights that enhancing control mechanisms is essential to the creation of intelligent and sustainable energy systems. It not only facilitates the integration of EVs into smart grids but also raises the general effectiveness of BWPT systems. Future studies in BWPT systems focus on enhancing the scalability and adaptability of the proposed dualphase shift Pulse Width Modulation (PWM) technology to accommodate various power ratings and frequencies. Analyzing the integration of innovative Artificial intelligence and machine learning are two examples of technologies that could aid in improving control strategies for increased system performance and efficiency. Additionally, looking into the potential integration of energy storage devices into the System reliability and grid stability may be enhanced by a bidirectional power transmission arrangement.

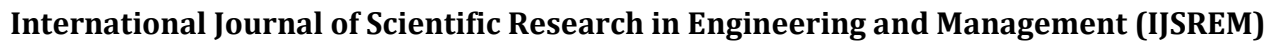
REFERENCES

- [1] M. Venkatesan, N. Rajamanickam, P. Vishnuram, M. Bajaj, V. Blazek, L. Prokop, and S. Misak, "A Review of compensation topologies and control techniques of bidirectional wireless power transfer systems for electric vehicle applications," Energies, vol. 15, no. 20, Oct. 1, 2022, doi: 10.3390/en15207816.
- [2] Q. He, Q. Luo, K. Ma, P. Sun, and L. Zhou, "Analysis and design of a single-stage bridgeless high-frequency resonant AC/AC converter," IEEE Trans. Power Electron., vol. 34, no. 1, pp. 700–711, Jan. 2019.
- [3] M.Kim,D.-M.Joo,andB.K.Lee, "Designandcontrolofinductive power transfer system for electric vehicles considering wide variation of output voltage and coupling coefficient," IEEE Trans. Power Electron., vol. 34, no. 2, pp. 1197–1208, Feb. 2019, doi: 10.1109/TPEL.2018.2835161.
- [4] X. Wang, J. Xu, M. Leng, H. Ma, and S. He, "A hybrid control strategy of LCC-S compensated WPT system for wide output voltage and ZVS range with

minimized reactive current," IEEE Trans. Ind. Electron., vol. 68, no. 9, pp. 7908–7920, Sep. 2021, doi: 10.1109/TIE.2020.3013788.

ISSN: 2582-3930

- [5] X. Qu, H. Chu, S.-C. Wong, and C. K. Tse, "An IPT battery charger with near unity power factor and loadindependent constant output combating voltage constraints of input and transformer parameters," IEEE Trans. Power Electron., vol. 34, no. 7719–7727, 2019, 8, pp. Aug. doi: 10.1109/TPEL.2018.2881207.
- [6] X. Liu, N. Jin, X. Yang, K. Hashmi, D. Ma, and H. Tang, "A novel single switch phase controlled wireless power transfer system," Electronics, vol. 7, no. 11, p. 281, Oct. 2018, doi: 10.3390/electronics7110281.
- [7] V. Shevchenko, O. Husev, R. Strzelecki, B. Pakhaliuk, N. Poliakov, and N. Strzelecka, "Compensation topologies in IPT systems: Standards, requirements, classification, analysis, comparison and application," IEEE Access, vol. 7, pp. 120559–120580, 2019.
- [8] D. Xu, C. Zhao, and H. Fan, "A PWM plus phase-shift control bidirec tional DC–DC converter," IEEE Trans. Power Electron., vol. 19, no. 3, pp. 666–675, May 2004, doi: 10.1109/TPEL.2004.826485. [9] R. Bosshard, J. W. Kolar, J. Mühlethaler, I. Stevanovic, B. Wunsch, and F. Canales, "Modeling and η – α -Pareto optimization of induc tive power transfer coils for electric vehicles," IEEE J. Emerg. Sel. Topics Power Electron., vol. 3, no. 1, pp. 50–64, Mar. 2015, doi: 10.1109/JESTPE.2014.2311302.
- [10] R. Bosshard and J. W. Kolar, "Inductive power transfer for elec tric vehicle charging: Technical challenges and tradeoffs," IEEE Power Electron. Mag., vol. 3, no. 3, pp. 22–30, Sep. 2016, doi: 10.1109/MPEL.2016.2583839.
- [11] M. Neath, "Bidirectional inductive power transfer system: Analysis and control," Ph.D. dissertation, Univ. Auckland, Auckland, New Zealand, 2013. [Online]. Available: http://hdl.handle.net/2292/22756
- [12] M. Mohammad, O. C. Onar, G.-J. Su, J. Pries, V. P. Galigekere, S. Anwar, E. Asa, J. Wilkins, R. Wiles, C. P. White, and L. E. Seiber, "Bidirec tional LCC–LCC-compensated 20-kW wireless power transfer system for medium-duty vehicle charging," IEEE Trans. Transport Electrific., vol. 7, no. 3, pp. 1205–1218, Sep. 2021, doi: 10.1109/TTE.2021.3049138.
- [13] S. A. Gorji, H. G. Sahebi, M. Ektesabi, and A. B. Rad, "Topolo gies and control schemes of bidirectional DC–DC power converters: An overview," IEEE Access,





SJIF Rating: 8.586 ISSN: 2582-3930

- vol. 7, pp. 117997–118019, 2019, doi: 10.1109/ACCESS.2019.2937239.
- [14] V. Juliet, S. Padmanaban, and L. Mihet-Popa, "Frequency splitting elimi nation and cross-coupling rejection of wireless power transfer to multiple dynamic receivers," Appl. Sci., vol. 8, no. 2, p. 179, Jan. 2018, doi: 10.3390/app8020179.
- [15] T. Taipei, X. Xu, A. M. Khambadkone, and R. Oruganti, "A soft-switched back-to-back Bi-directional DC/DC converter with a FPGA based digital control for automotive applications," in Proc. 33rd Annu. Conf. IEEE Ind. Electron. Soc., 2007, pp. 262–267.
- [16] K. Colak, E. Asa, M. Bojarski, D. Czarkowski, and O. C. Onar, "A novel phase-shift control of semibridgeless active rectifier for wireless power transfer," IEEE Trans. Power Electron., vol. 30, no. 11, pp. 6288–6297, Nov. 2015, doi: 10.1109/TPEL.2015.2430832.
- [17] H. Wu, Y. Lu, T. Mu, and Y. Xing, "A family of soft-switching DC–DC converters based on a phase-shift-controlled active boost rectifier," IEEE Trans. Power Electron., vol. 30, no. 2, pp. 657–667, Feb. 2015, doi: 10.1109/TPEL.2014.2308278.
- [18] H. Xiao and S. Xie, "A ZVS bidirectional DC–DC converter with phase shift plus PWM control scheme," IEEE Trans. Power Electron., vol. 23, no. 2, pp. 813–823, Mar. 2008, doi: 10.1109/TPEL.2007.915188.
- [19] Y. Yang, Y. Benomar, M. El Baghdadi, O. Hegazy, and J. Van Mierlo, "Design, modeling and control of a bidirectional wireless power transfer for light-duty vehicles: G2 V and V2G systems," in Proc. 19th Eur. Conf. Power Electron. Appl., Sep. 2017, pp. P1–P12, doi: 10.23919/EPE17ECCEEurope.2017.8099387. [20] S. Liu, J. Su, and J. Lai, "Accurate expressions of mutual inductance and their calculation of Archimedean spiral coils," Energies, vol. 12, no. 10, p. 2017, May 2019, doi: 10.3390/en12102017. [21] K. Aditya, "Analytical design of Archimedean spiral coils used in induc tive power transfer for electric vehicles application," Electr. Eng., vol. 100, no. 3, pp. 1819–1826, Sep. 2018, doi: 10.1007/s00202-017-0663-7.
- [22] Y. Yang, J. Cui, and X. Cui, "Design and analysis of magnetic coils for optimizing the coupling coefficient in an electric vehicle wireless power transfer system," Energies, vol. 13, no. 16, p. 4143, Aug. 2020, doi: 10.3390/en13164143.
- [23] X.Liu, C. Xia, and X. Yuan, "Study of the circular flat spiral coil structure effect on wireless power transfer system performance," Energies, vol. 11, no. 11, p. 2875, Oct. 2018, doi: 10.3390/en11112875. [24] A. Garcia-

- Bediaga, A. Avila, I. Alzuguren, A. Sanchez, and A. Rujas, "Power factor corrector control strategies of a bidirectional wireless bat tery charger with an unfolding active rectifier," IEEE J. Emerg. Sel. Topics Power Electron., vol. 11, no. 1, pp. 396–406, Feb. 2023, doi: 10.1109/JESTPE.2022.3164720. [25] X. Wang, M. Leng, L. He, and S. Lu, "An improved LCC-S compen sated inductive power transfer system with wide output voltage range and unity power factor," IEEE Trans. Transport. Electrific., early access, doi: 10.1109/TTE.2023.3297623.
- [26] T. Bouanou, H.ElFadil, A. Lassioui, O. Assaddiki, and S. Njili, "Analysis of coil parameters and comparison of circular, rectangular, and hexagonal coils used in WPT system for electric vehicle charging," World Electric